

Average Brightness Temperature of Lunar Surface for Calibration of Multichannel Millimeter-Wave Radiometer From 89 to 183 GHz and Data Validation

Niutao Liu¹, *Student Member, IEEE*, and Ya-Qiu Jin¹, *Life Fellow, IEEE*

Abstract—Calibration of satellite-borne radiometer is a key issue for quantitative remote sensing. Its accuracy depends on the stability of the calibration source. Because of no atmosphere and biological activity, the Moon surface keeps stable in the long term and may be a good candidate for thermal calibration. Observation of microwave humidity sounder (MHS) onboard the NOAA-18 made measurements of the disk-integrated brightness temperature (TB) of the Moon for the phase angle between -80° and 50° . The measurement of NOAA-18 has been studied to validate the TB model of lunar surface. In this article, the near side of the Moon surface is divided into 900 subregions with a span of $6^\circ \times 6^\circ$ in longitude and latitude. By solving 1-D heat conductive equation with the thermophysical parameters validated by the Diviner data of the Lunar Reconnaissance Orbiter (LRO), the temperature profiles of the regolith media in all 900 subregions are obtained. The loss tangents are inverted from the Chang’e-2 (CE-2) 37-GHz microwave TB data at noontime. Employing the fluctuation-dissipation theorem and the Wentzel-Kramers-Brillouin (WKB) approach, the microwave and millimeter-wave TBs of each subregion are simulated. Then, the weighted average TB can be disk-integrated from 900 TBs of all subregions versus the phase angle. These simulations well demonstrate diurnal TB variation and its dependence upon the frequency channels. It is found that the disk-integrated TB of the Moon in MHS channels is sensitive to the full-width at half-maximum (FWHM) of the deep space view (DSV), which is corrected in our simulation, where the Moon is now taken as an extended target, instead of a point-like object. Simulated integrated TBs are compared with the corrected MHS TB data at 89, 157, and 183 GHz. The simulated TB is well consistent with these MHS TB data at 89 and 183 GHz at various phase angles. But the maximum TB of MHS data at 157 GHz is unusually lower than that of 89 GHz. The influence of the loss tangent, emissivity, and the pointing error is analyzed. Some more careful design to observe the Moon TB and technical parameters, especially the FWHM should be well determined. Our model and numerical simulation provides a tool for TB calibration and validation.

Index Terms—Meteorological satellite, millimeter-wave calibration, thermal emission of the Moon.

I. INTRODUCTION

CALIBRATION of satellite-borne radiometer is a key issue for quantitative remote sensing. Due to the lack of a stable reference target, long-term drift on orbit may degrade the calibration accuracy [1]. Because there is no atmosphere, biological activity, and quick geological variation, the Moon surface keeps stable physically and chemically in the long term. Thus, the nearside of the Moon is seen as a potential calibration source for meteorological satellites [2].

The ground-based observation of microwave brightness temperature (TB) of the Moon could be pursued to the 1940s [3]. It was difficult to interpret those TB because of very limited knowledge about physical properties at that time. Advances of the satellite-borne remote sensing, for example, the infrared (IR) Lunar Reconnaissance Orbiter (LRO) program, present the feasibility to quantitatively analyze the thermophysical properties. The Diviner Lunar Radiometer Experiment onboard LRO measured the global mid-IR irradiance [4]. Lunar surface temperatures at night were used to constrain the thermophysical properties of the lunar regolith media [5]. By solving the 1-D heat conductive equation, the temperature profile of the media was retrieved as well. The temperature at the regolith depth was also validated by the Apollo heat measurement. It turns to validate the constrained thermophysical properties [6]. This approach is also applied to the simulation of the microwave and millimeter-wave TB [2]. Microwave can penetrate through the regolith media. The inversion analysis of Chinese Chang’e-2 (CE-2) microwave data is applicable to the study of the dielectric constants of the regolith media, especially the loss tangents [2], [7], [8]. The inverted loss tangents were fit against the TiO_2 abundance and were applied to the simulation of global millimeter wave TB.

It was reported that the NOAA-18 was launched on May 20, 2005, and the observation of microwave humidity sounder (MHS) onboard was occasionally corrupted by the presence of the Moon in its deep space view (DSV). Measurements of the disk-integrated TB of the Moon at 89, 157, and 183 GHz were presented for the phase angles

Manuscript received September 24, 2019; revised December 25, 2019, February 21, 2020, and May 9, 2020; accepted June 1, 2020. This work was supported in part by the National Key Research and Development Program of China under Grant 2017YFB0502703 and in part by the Fudan Outstanding Doctor Fellowship under Grant SSH6281011. (Corresponding author: Ya-Qiu Jin.)

The authors are with the Key Laboratory for Information Science of Electromagnetic Waves (Ministry of Education), Fudan University, Shanghai 200433, China (e-mail: yqjin@fudan.edu.cn).

Color versions of one or more of the figures in this article are available online at <http://ieeexplore.ieee.org>.

Digital Object Identifier 10.1109/TGRS.2020.3000230

0196-2892 © 2020 IEEE. Personal use is permitted, but republication/redistribution requires IEEE permission. See <https://www.ieee.org/publications/rights/index.html> for more information.

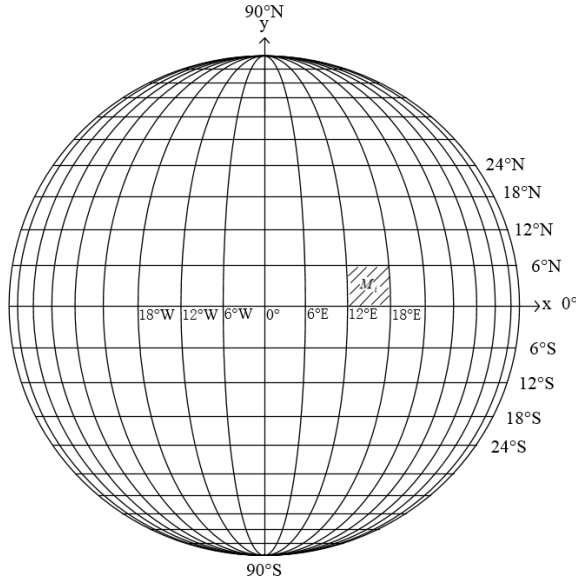


Fig. 1. Meshed subregion of the lunar surface.

between -80° and 50° relative to the full Moon (the phase angle is 0°) [9] when the Moon happened to appear in the MHS DSV.

In this article, the disk-integrated millimeter-wave TB is numerically studied for quantitative analysis. The whole near side of the Moon is equally meshed into subregions of $6^\circ \times 6^\circ$ in the latitude and longitude, as shown in Fig. 1. There are totally $30 \times 30 = 900$ subregions. The temperature profile of these subregions is numerically simulated based on the Diviner constrained thermophysical properties [6]. Using the radiative transfer of the fluctuation-dissipation theorem and the Wentzel-Kramer-Brillouin (WKB) approach with the loss tangents of the regolith, the microwave and millimeter-wave TBs of all subregions are calculated. The weighted average disk-integrated TB is obtained. As the Moon is now taken as an extended target, via the simulations, the full-width at half-maximums (FWHMs) of the MHS channels at 89, 157, and 183 GHz are corrected. The integrated TB of the Moon from the MHS data are then corrected and compared with the simulated TBs. The effect of the pointing error on the disk-integrated TB of the Moon is also simulated [9]. The influence of regolith loss tangent and the emissivity on the simulated TB are analyzed.

This article is organized as follows. Section II introduces the derivation of physical temperature profiles of all subregions by solving the 1-D heat conductive equation. Section III presents the average disk-integrated microwave TB. In Section IV, the FWHM and the disk-integrated TB of the Moon from the MHS data are corrected and compared with the simulation. In Section V, the effect of the pointing error, the influences of the regolith loss tangent, and the emissivity are analyzed. Finally, Section VI gives conclusion.

II. PHYSICAL TEMPERATURE OF SUBREGOLITH

A. Heat Conduction Model

The nearside of the Moon is meshed into 30×30 subregions with a span of $6^\circ \times 6^\circ$ in latitude and longitude. The longitude

of the near side of the Moon ranges from 90° W to 90° E, as shown in Fig. 1. The surface temperatures of all these subregions are calculated by solving the 1-D heat conductive equation. The topography of each subregion is ignored. The incline of the lunar orbit, about $5^\circ 9'$ from the orbit plane of the Earth, is ignored as well.

The phase angle is usually defined as the angle between the observer's line of sight and the line of solar illumination impinging on the Moon. The Moon rotates with a fixed nearside facing the Earth. The phase angle, related with the subsolar longitude, is adopted to describe the local time at the equator center (0° N, 0° E), which is the center of the nearside. A phase angle of 0° corresponds to the noon by lunar local time at the equator center. A change of 1 h by lunar local time is 15° in phase angle.

To obtain the temperature profile of the regolith media of each subregion, 1-D heat conductive equation of this subregion is written as [10]

$$\rho C \frac{\partial T}{\partial t} = \frac{\partial}{\partial z} \left(K \frac{\partial T}{\partial z} \right) \quad (1)$$

where $T(z)$ is the temperature profile, t is the time, z is the depth, K is the thermal conductivity, $\rho(z)$ is the bulk density of the media, and C is the heat capacity.

Based on the measurement of lunar samples and the constraints of the Diviner data, the density profile $\rho(z)$ of the regolith is written as [6]

$$\rho(z) = \rho_d - (\rho_d - \rho_s)e^{-z/H} \quad (2)$$

where $\rho_s = 1100 \text{ kg m}^{-3}$ and $\rho_d = 1800 \text{ kg m}^{-3}$. H is set to be 6 cm.

The heat capacity $C(T)$ of the regolith is dependent on the temperature and is fit as [6], [11], [12]

$$C = C_0 + C_1 T + C_2 T^2 + C_3 T^3 + C_4 T^4 \quad (3)$$

where $C_0 = -3.6125 \text{ J kg}^{-1} \text{ K}^{-1}$, $C_1 = +2.7431 \text{ J kg}^{-1} \text{ K}^{-2}$, $C_2 = +2.3616 \times 10^{-3} \text{ J kg}^{-1} \text{ K}^{-3}$, $C_3 = -1.2340 \times 10^{-5} \text{ J kg}^{-1} \text{ K}^{-4}$, and $C_4 = +8.9093 \times 10^{-9} \text{ J kg}^{-1} \text{ K}^{-5}$.

The heat conductivity $K(T)$ of the regolith consists of solid phonon conductivity and radiative conductivity [13]

$$K = K_c \left[1 + \chi \left(\frac{T}{350} \right)^3 \right] \quad (4)$$

where the radiative conductivity parameter χ is 2.7 [6] and K_c is the solid phonon conductivity. Based on the measurement of [13], K_c is assumed to be linearly proportional to the density [6]

$$K_c = K_d - (K_d - K_s) \frac{\rho_d - \rho}{\rho_d - \rho_s} \quad (5)$$

where $K_s = 7.4 \times 10^{-4} \text{ W m}^{-1} \text{ K}^{-1}$ and $K_d = 3.4 \times 10^{-3} \text{ W m}^{-1} \text{ K}^{-1}$. K_s is the heat conductivity at the surface, and K_d is the heat conductivity at the depth.

The boundary conditions of (1) are written as

$$K(z, T) \frac{\partial T}{\partial z} \Big|_{z=0} = \text{TSI}(1 - A) \cos^+ \theta_i - e \sigma_0 T_s^4 - J_0 \quad (6a)$$

$$K(z, T) \frac{\partial T}{\partial z} \Big|_{z=-\infty} = -J_0 \quad (6b)$$

where the bolometric IR emissivity of lunar surface, e , is set to be 0.95 [6]. T_s is the surface temperature, σ_0 is the Stefan–Boltzmann constant, and J_0 is set to 0 W/m², which is a negligible constant heat flux originating from internal heat source (global measurement is not yet available). The total solar irradiance (TSI) is the solar irradiance received by the Moon. Here, TSI is set to be 1371 W/m², which corresponds to the distance of 1 astronomical unit (AU) between the Sun and the Moon [14]. The topographic perturbation of each subregion is ignored. θ_i is the incident angle of sunlight. $\cos^+ \theta_i$ is equal to $\cos \theta_i$ when θ_i is less than 90° during day time. Otherwise, $\cos^+ \theta_i$ is zero. Suppose that the longitude of each local region is λ_0 and the latitude is φ_0 , the subsolar longitude is λ and the subsolar latitude is φ . In the principal coordinate system ($\hat{x}_0, \hat{y}_0, \hat{z}_0$), \hat{z}_0 is the unit vector from the Moon center to the north pole and \hat{x}_0 is the unit vector from the Moon center to the lunar equator center (both of the longitude and latitude are 0°). The axis \hat{z}_l is the unit vector from the Moon center to the local region point and can be written as [15]

$$\hat{z}_l = \cos \varphi_0 \cdot \cos \lambda_0 \cdot \hat{x}_0 + \cos \varphi_0 \cdot \sin \lambda_0 \cdot \hat{y}_0 + \sin \varphi_0 \cdot \hat{z}_0. \quad (7)$$

The unit vector from the Moon center to the subsolar point can be written as

$$\hat{s} = \cos \varphi \cdot \cos \lambda \cdot \hat{x}_0 + \cos \varphi \cdot \sin \lambda \cdot \hat{y}_0 + \sin \varphi \cdot \hat{z}_0. \quad (8)$$

The local incidence angle of solar illumination can be obtained as

$$\cos \theta_i = \hat{z}_l \cdot \hat{s}. \quad (9)$$

Ignoring the tilt of the rotation axis, the subsolar latitude is set to be 0°. The subsolar longitude is assumed to change at a constant speed in a lunation (about 29.53 Earth day) [8].

The albedo of lunar surface A depends on the solar incident angle θ_i and is fit as follows [16]:

$$A(\theta) = A_0 + a(\theta_i/45)^3 + b(\theta_i/90)^8 \quad (10)$$

where A_0 is the normalized albedo. A_0 can be obtained by dividing Clementine 750-nm data with a factor of 1.3 to an average solar wavelength. The albedo is consistent with the result derived from Diviner's broadband solar channels [5]. The parameters $a = 0.06$ and $b = 0.25$ are two empirical coefficients [6]. The average A_0 of each region derived from Clementine data is used as the input of the upper boundary of the heat conductive equation.

The Moon is assumed to be an ideal sphere. By applying the numerical finite-difference time-domain (FDTD) method to solve (1) and (6), the temperature profile $T(z)$ can be obtained [2]. The initial temperature is set to be 250 K. The time step is set to be 36 s and each temperature profile is obtained after running the FDTD code for 300 lunations. Parallel computation is used and the total computation time of the temperature profile is 40 h. Nonlinear subdivision is used to discretize the depth [6]. The space step of $\Delta z(n) = 0.00005 \times (n - 1) + 0.001$ is used as the size of each cell, where n is the number of the cell. There are totally 190 cells, and the depth in the calculation is 1.09 m.

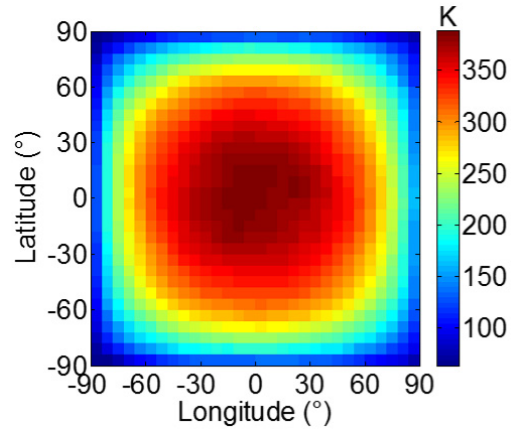


Fig. 2. Surface temperature of the full Moon.

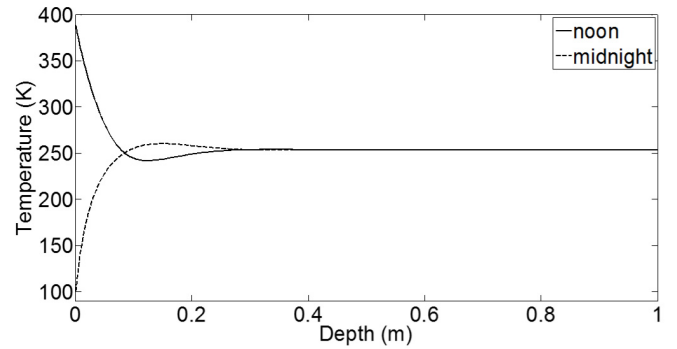


Fig. 3. Temperature profiles of the equator center at noon and midnight.

The simulated surface temperature can be validated by the Diviner IR data at T_7 channel (25–41 μm) [2]. The simulated temperature at a depth of 1.3 m is consistent with the measurement of the Apollo heat experiment as well [2]. The validation makes sure that the simulated temperature can be adopted for microwave and millimeter-wave TB calculation.

The surface temperature of the full moon is shown in Fig. 2. The incidence angle of the Sun light at the equator center is the smallest at the full moon. It is the noontime in lunar local time at the equator center. The surface temperature reaches the peak value at noontime when the incident angle of Sun light is the minimum because of the heat balance [14].

In [1], by directly multiplying a mean surface temperature with an emissivity to obtain TB, the peak value of the TB appeared exactly at the full moon. Since microwave can penetrate into the regolith, the temperature of the regolith beneath the surface keeps increasing for a while after the noontime. Thus, the TB peak appears after the noon. A low frequency corresponds to a large phase angle of TB peak [2].

The temperature profiles of the equator center at noon and at night are shown in Fig. 3. At noon, temperature decreases rapidly with the depth increase. A small penetration depth of high-frequency leads to a large TB at daytime. The temperature profile is inversed at night. So, the TB of high frequency becomes small at night.

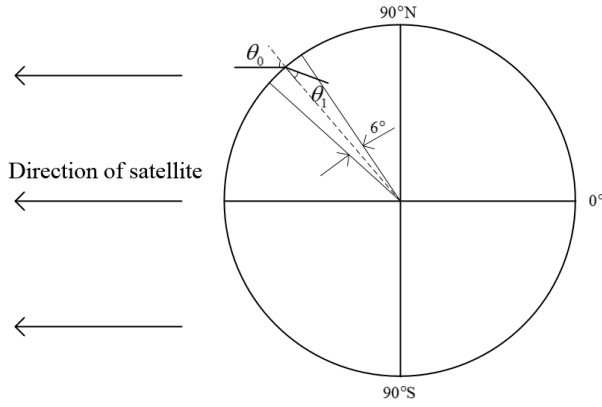


Fig. 4. Emission angle and the refraction angle.

III. RADIATIVE TRANSFER MODEL FOR MICROWAVE TB

The depth of the regolith is much larger than the penetration depth of 89 GHz or higher frequency [17]–[19]. The regolith is modeled as a half-space [8]. Based on the fluctuation–dissipation theorem and the WKB approach, the TB from a uniformly inhomogeneous medium can be obtained as [20], [21]

$$T_B(\theta_0) = [1 - \Gamma(\theta_0)] \int_0^\infty \sec \theta_1 \kappa_a(z) T(z) e^{-\int_0^z \kappa_a(z') \sec \theta_1 dz'} dz \quad (11)$$

where the emission angle θ_0 is the observation angle, that is, the angle between the normal of the local surface and the vector from the surface to the satellite. θ_1 is the refraction angle in the regolith as shown in Fig. 4. The relationship between θ_0 and θ_1 meets the Snell law. $1 - \Gamma(\theta_0)$ and $\Gamma(\theta_0)$ are the Fresnel emissivity and the reflectivity of flat surface of each subregion. $\Gamma(\theta_0)$ is the average of the horizontal and vertical polarization reflectivity

$$\Gamma(\theta_0) = (\Gamma_h(\theta_0) + \Gamma_v(\theta_0))/2 \quad (12)$$

where

$$\Gamma_h(\theta_0) = \left(\frac{\sqrt{\varepsilon_0} \cos \theta_0 - \sqrt{\varepsilon_s} \cos \theta_1}{\sqrt{\varepsilon_0} \cos \theta_0 + \sqrt{\varepsilon_s} \cos \theta_1} \right)^2 \quad (13a)$$

$$\Gamma_v(\theta_0) = \left(\frac{\sqrt{\varepsilon_s} \cos \theta_0 - \sqrt{\varepsilon_0} \cos \theta_1}{\sqrt{\varepsilon_s} \cos \theta_0 + \sqrt{\varepsilon_0} \cos \theta_1} \right)^2 \quad (13b)$$

where ε_s is the surface dielectric constant of each subregion. The absorption coefficient of the regolith media, κ_a , is written as

$$\kappa_a = \frac{2\pi \nu \varepsilon''(z)}{c \sqrt{\varepsilon'(z)}} \quad (14)$$

where ν is the frequency, c is the light speed in free space, and $\varepsilon'(z)$ and $\varepsilon''(z)$ are the real and imaginary parts of the dielectric constant at the depth z , respectively.

The dielectric constant of regolith mainly depends on the volume of void space [18]. The real part of the dielectric constant $\varepsilon'(z)$ is fit against the porosity $n(z)$ and specific gravity g by the Maxwell–Garnett formula [8]

$$\frac{1}{\langle \rho \rangle} \frac{\langle \varepsilon \rangle - 1}{\langle \varepsilon \rangle + 2} = \frac{1}{(1 - n(z))g} \frac{\varepsilon'(z) - 1}{\varepsilon'(z) + 2} \quad (15)$$

where $\langle \varepsilon \rangle = 2.75$ and $\langle \rho \rangle = 1.7 \text{ g/cm}^3$. The dielectric constant $\varepsilon'(z)$ of regolith media is determined by (15) when porosity profile $n(z)$ and specific gravity g are obtained.

The loss tangent of the regolith is a key parameter for calculation of microwave TB. It mainly depends on the TiO_2 abundance [18]. But there were only 23 samples for data fitting in [18] and only three samples are with the TiO_2 abundance more than 4 wt.% [18]. It is noted that the TiO_2 abundance at Maria is usually larger than 4 wt.%.

Thus, instead of fitting the loss tangent of few samples, the microwave TB data of CE-2 at 37 GHz (TB_{37}) along the equator at the noon are collected to invert the loss tangent at each longitude [2]. Then, the parameters, p_1 and p_2 , can be chosen to fit the loss tangent against TiO_2 abundance as [2]

$$\tan \delta = p_1 \text{TiO}_2 + p_2$$

$$p_1 = 3.516 \times 10^{-4}, \quad p_2 = 0.0087 \text{ as } \text{TiO}_2 > 1\%$$

$$p_1 = -8.945 \times 10^{-5}, \quad p_2 = 0.0097 \text{ as } \text{TiO}_2 < 1\%. \quad (16)$$

Most of the TiO_2 abundance at highland is less than 1% while more than 1% at Maria. So, the loss tangent is fit separately for $\text{TiO}_2 < 1\%$ and $\text{TiO}_2 > 1\%$. The results of (16) are in the range of the sample measurement [2]. Based on the average TiO_2 abundance of each subregion, the loss tangents of total 900 subregions are obtained.

The porosity profile of the regolith is derived from the measurements of regolith samples collected at Apollo landing sites [18]

$$n(z) = 1 - \frac{1.919}{g_0} \frac{z + 0.122}{z + 0.18} \quad (17)$$

where $g_0 = 3.1 \text{ g/cm}^3$ is the nominal specific gravity (bulk density without void). The porosity of (17) is adopted in simulations.

Based on the sample measurement, the specific gravity is fit against the mineral abundance of the samples [22]

$$g = 27.3\text{FeO} + 11\text{TiO}_2 + 2773 \quad (18)$$

where g is in kilogram per cubic meter. FeO and TiO_2 are the percentage of minerals by weight, which can be derived from Clementine data [23]. The average FeO and TiO_2 abundance is used to derive the real part of the dielectric constant in each subregion.

First, the TB simulation is validated by CE-2 TB_{37} at the equator and at 60°N [2]. The TBs from all subregions contribute to the average disk-integrated TB of the Moon. The coverage of each subregion seen from the satellite, as shown in Fig. 1, can be written as

$$\begin{aligned} M_i &= \frac{R^2}{D^2} \int_{\varphi_{i2}}^{\varphi_{i1}} (\sin \lambda_{i2} - \sin \lambda_{i1}) \cos \varphi \cdot d(\sin \varphi) \\ &= \frac{R^2}{D^2} \cdot |\sin \lambda_{i2} - \sin \lambda_{i1}| \\ &\quad \cdot \left[\frac{1}{2}(\varphi_{i1} - \varphi_{i2}) + \frac{1}{4}(\sin(2\varphi_{i1}) - \sin(2\varphi_{i2})) \right] \end{aligned} \quad (19)$$

where $R = 1737.4 \text{ km}$ is the radius of the Moon. D is the distance between the satellite and the Moon and is set to be 380 000 km. λ_{i1} and λ_{i2} are the longitudes of the

left and right boundaries, respectively, of the subregion in arc. φ_{i1} and φ_{i2} are the latitudes of the upper and lower boundaries, respectively. It is noted that M_i is the coverage of the i th subregion in the view of satellite observation, instead of the whole coverage of subregion i . In the same way as [9], the weighted average disk-integrated TB of the nearside of the Moon can be observed and written as

$$\bar{T}_{BW} = \frac{\sum_i T_{Bi}(\theta_{0i}) G_i \cdot M_i}{\sum_i G_i \cdot M_i} \quad (20)$$

where $T_{Bi}(\theta_{0i})$ is the TB of the i th subregion (i ranges from 1 to 900) from (11). θ_{0i} is the observation angle to this subregion. G_i is the antenna response function and can be written as [9]

$$G_i = \frac{1}{2\pi\sigma^2} e^{-\frac{x_i^2 + y_i^2}{2\sigma^2}} \quad (21)$$

where

$$\sigma = \frac{\text{FWHM}}{2\sqrt{2\ln(2)}} \quad (22)$$

here the unit of σ is arc. When the center of the DSV overlaps the center of the Moon, there is

$$x_i = \frac{R}{D} \cdot \cos\left(\frac{\varphi_{i1} + \varphi_{i2}}{2}\right) \cdot \sin\left(\frac{\lambda_{i1} + \lambda_{i2}}{2}\right) \quad (23a)$$

$$y_i = \frac{R}{D} \cdot \sin\left(\frac{\varphi_{i1} + \varphi_{i2}}{2}\right). \quad (23b)$$

Fig. 5 shows $T_{Bi}(\theta_{0i})$ of the near side of the Moon when the \bar{T}_{BW} reaches the peak. The Moon locates at the center of the DSV. At higher frequency, larger TB peak can be reached. For example, the frequency 157 GHz is much higher than 89 GHz. The maximum TB of 157 GHz is larger than that of 89 GHz by about 15 K. The maximum TB of 183 GHz is a little higher than that of 157 GHz by about 3 K. When the observation angle becomes large, the observed TB is significantly reduced. It leads to a small $T_{Bi}(\theta_{0i})$ from the edge of the near side of the Moon.

IV. DATA VALIDATION AND ANALYSIS

A. Correction of FWHM

Based on the MHS observation, the spectral radiance of the Moon can be derived as [9]

$$B_v^{\text{Moon}} = \frac{s}{G_A \eta F_{\text{ch}}} + B_v^{\text{CMB}} \quad (24)$$

where s is the difference of the number of counts with and without the Moon in the center of the field of view. G_A is the gain of the instrument in counts per unit of spectral radiance. η is the beam efficiency measured on the ground. F_{ch} is the fraction of the beam covered by the Moon. B_v^{CMB} is the spectral radiance of the cosmic microwave background. The digital count in level 1b data set from MHS is used. The spectral radiance is converted to the TB of the Moon with an inverse Planck function. The phase angle of the MHS observation with NOAA-18 ranges from -80° to 50° [9].

As Burgdorf *et al.* [9] pointed out, the parameter F_{ch} in (24) is important for the calculated Moon radiance, but has little influence on the phase angle of the peak \bar{T}_{BW} . The estimated

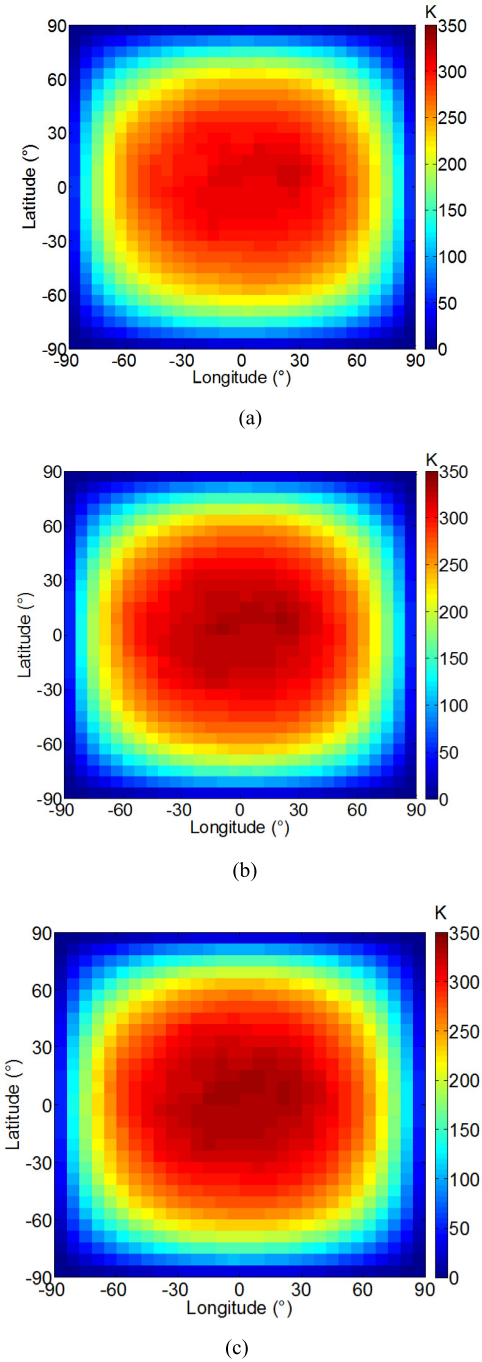


Fig. 5. $T_B(\theta_{0i})$ of the Moon disk when \bar{T}_{BW} reaches its peak. The Moon locates at the center of the DSV. (a) 89, (b) 157, and (c) 183.3 GHz.

FWHM from the DSV counts determines the F_{ch} . To estimate the FWHM, the Moon was treated as a point target [9]. It may overestimate FWHM. Thus, the FWHM value in DSV for the integrated Moon should be remodified.

The MHS counts were used to fit the FWHM. It can be seen that $s/(G_A \cdot \eta)$ corresponds to the antenna temperature while $s/(G_A \cdot \eta \cdot F_{\text{ch}})$ corresponds to the disk-average TB. When the Moon appears in the DSV, the counts of cosmic background should be subtracted [9]. So, the radiance out of the coverage of the Moon is zero. With the scanning of DSV, the antenna

temperature (in unit of K) of the observed lunar disk with subtraction of the cosmic background radiance, which can be derived by applying an inverse Planck transform to spectrum irradiance, is written as

$$T_a(d) = \iint_{A_{\text{Moon}}} (T_B(x, y) - T_{\text{BC}}) \cdot G(x, y, d) dx dy \quad (25)$$

where A_{Moon} is the coverage of the Moon. d is the span angle between the center of the DSV and the center of the Moon, in unit of arc. T_{BC} is the radiance of the cosmic background and is set to be 2.73 K. The unit of $T_a(d)$ is kelvin. Correspondingly, applying an inverse Planck transform to $s/(G_A \cdot \eta \cdot F_{\text{ch}})$, the disk-average TB in (20) can be obtained.

In a discrete form, (25) can be written as

$$T_a(d) = \sum_i (T_{B_i}(\theta_{0i}) - T_{\text{BC}}) \cdot G_{id}(d) \cdot M_i. \quad (26)$$

The antenna response function is written as

$$G_{id}(d) = \frac{1}{2\pi\sigma^2} e^{-\frac{(x_i-d)^2+y_i^2}{2\sigma^2}} \quad (27)$$

where σ is defined in (22). x_i and y_i are given in (23). The span angle between the center of the DSV and the center of the Moon is incorporated in the antenna response function. The step of d is set to be $0.001\pi/180$. When the Moon passes through the center of the DSV, it is assumed that the θ_{0i} and T_{B_i} in (26) are unchanged.

When the weighted average TB reaches the maximum and minimum, the TB distribution of the Moon is applied to estimate the FWHM. The estimated FWHM in two cases is slightly different. The directly measured FWHM_{ch} from the observed data at 89, 157, and 183 GHz are 1.2° , 1.09° , and 1.25° , respectively [9].

It is assumed that the antenna response function is a 2-D Gaussian profile [9]. By setting a FWHM to the Gaussian profile, the $T_a(d)$ can be simulated with (26) when the Moon moves across the center of the DSV. The FWHM of the $T_a(d)$ can be measured. When the FWHM of the simulated $T_a(d)$ is almost the same as the measured FWHM_{ch} , the FWHM which has been set to the Gaussian function is taken as the corrected FWHM ($\text{FWHM}_{\text{ch}}^c$).

Fig. 6(a)–(c) shows the simulation of the $T_a(d)$ of (26) with assigned FWHM of 1.162° , 1.046° , and 1.213° , respectively. The FWHM measured from the simulated $T_a(d)$ are indicated by dotted lines in Fig. 6, which are very close to the directly measured FWHM_{ch} from MHS observation as aforementioned [9]. In the simulation, the corrected $\text{FWHM}_{\text{ch}}^c$ of 1.162° , 1.046° , and 1.213° at 89, 157, and 183 GHz are obtained, where the Moon is taken as an extended target.

The distance D between the Moon and the satellite is in the range of about 405 000 and 360 000 km between apogee and perigee, respectively [2]. In this article, the distance D is set to be a middle value, 380 000 km. The variation of D may affect the $\text{FWHM}_{\text{ch}}^c$ up to about $\pm 0.005^\circ$. The T_{B_i} of lunar disk at different phase angle can also affect the $\text{FWHM}_{\text{ch}}^c$, as shown in Fig. 6(a)–(c). It is found that the difference between the $\text{FWHM}_{\text{ch}}^c$ and measured FWHM ($\sim 1.58^\circ$) is about 0.02° by deconvolution [24] while the difference is about 0.04° in this article. This may be caused by a large FWHM. Take the

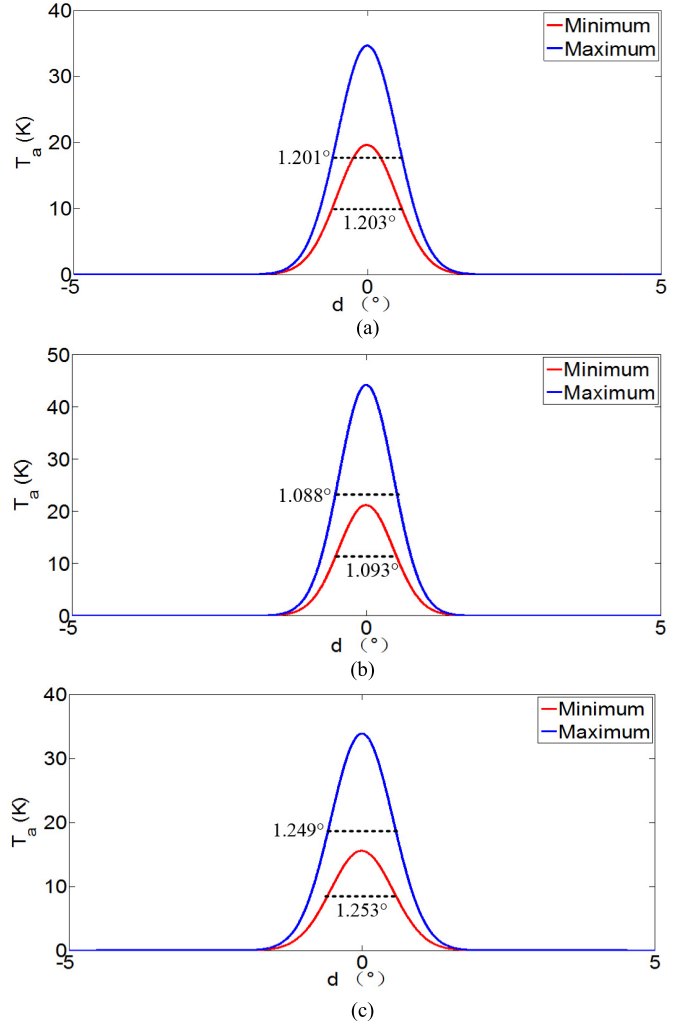


Fig. 6. Simulated FWHM. The horizontal axis is the distance between the center of DSV and the center of the Moon (the unit is converted to degree). “Minimum” in the legend means the TB distribution when the \bar{T}_{BW} is the minimum and “Maximum” in the legend means the TB distribution when the \bar{T}_{BW} is the maximum. (a) 89, (b) 157, and (c) 183 GHz.

simulated T_{B_i} at 89 GHz as an example when \bar{T}_{BW} is the maximum. By setting a $\text{FWHM}_{\text{ch}}^c$ of 1.56° , the simulated FWHM is 1.585° with $D = 405\,000$ km. The result is similar with [24].

B. Correction of Data and Analysis

F_{ch} in (24) can be written as [9]

$$F_{\text{ch}} = 1 - e^{-4 \ln 2 \cdot r_{\text{Moon}}^2 / \text{FWHM}_{\text{ch}}^2} \quad (28)$$

where r_{Moon} is the span angle of the Moon radius and can be written as R/D . R is the radius of the Moon, and D is the distance between the satellite and the Moon. The unit of r_{Moon} is arc. In calculation, the unit of FWHM_{ch} should be written into arc as well. Based on the Rayleigh–Jeans law and (24), the corrected disk-integrated TB data can be written as

$$T_B^c = (T_B^M - T_{\text{BC}}) \cdot \frac{F_{\text{ch}}}{F_{\text{ch}}^c} + T_{\text{BC}} \quad (29)$$

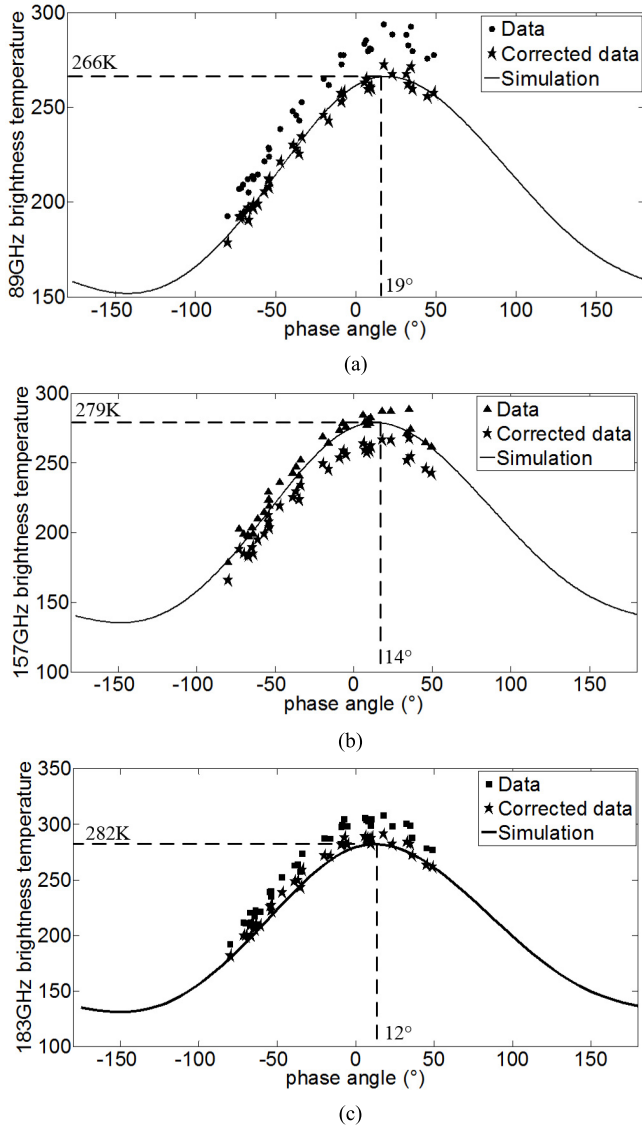


Fig. 7. Simulated \bar{T}_{BW} , the MHS data, and the corrected MHS data derived from MHS observation. (a) 89, (b) 157, and (c) 183 GHz.

where T_B^M is the calculated disk-integrated TB data in [9] and F_{ch} is derived from the $FWHM_{ch}$ [9]. F_{ch}^c is derived with (28) using the corrected $FWHM_{ch}^c$.

The MHS TB data from [9], the corrected MHS TB data with (29), and the simulated \bar{T}_{BW} are shown in Fig. 7(a)–(c).

It can be seen in Fig. 7(a)–(c) that the simulated \bar{T}_{BW} reaches the peak at the phase angle of 19°, 14°, and 12° at 89, 157, and 183 GHz, respectively. It means that the higher frequency channel can more quickly reach the peak.

The peak values of these three channels are about 266, 279, and 282 K, respectively. Big difference between the frequencies yields big difference of the TB peaks. It is noted that high-frequency channel has small penetration depth. Both of the TB peak and the phase angle are more sensitive to the temperature of the top regolith layer at high frequency.

Table I lists the peak values of these three data sets. Via the correction of FWHM, the corrected MHS data at 89 and 183 GHz are well consistent with the simulated \bar{T}_{BW} .

TABLE I
MHS TB PEAKS OF FIG. 7(a)–(c)

Frequency	T_B^M peak [9]	Corrected T_B^c peak	Simulated TB peak	FWHM in simulation
89GHz	$288 \pm 4K$	$271 \pm 4K$	266K	1.2°
157GHz	$285 \pm 6K$	$264 \pm 6K$	279K	1.09°
183GHz	$303 \pm 5K$	$286 \pm 5K$	282K	1.25°

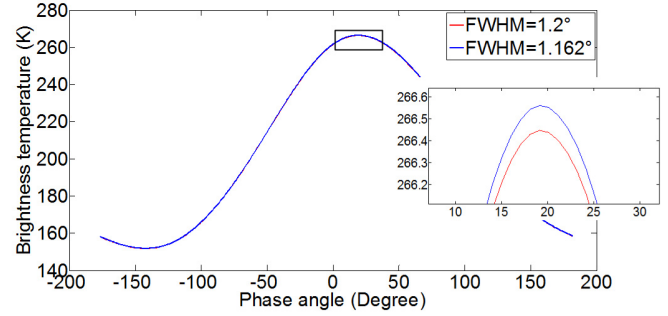


Fig. 8. Influence of FWHM on the simulated TB at 89 GHz.

However, the corrected MHS TB at 157 GHz seems questionable because it is much lower than the \bar{T}_{BW} .

In Fig. 7(a)–(c), it can be seen that a higher frequency has smaller TB peak phase shift. For example, the phase angle at 157 GHz is about 14° and is smaller than 19° of 89 GHz. A smaller penetration depth of higher frequency presents a higher TB peak.

The contradiction of the TB value at 157 GHz is likely to be caused by the real situation in observation because the phase angle of the TB peak is consistent with the simulation. Some technical and physical parameters, for example, FWHM, beam efficiency, and so on, need further study.

In simulation, it can be found that the uncertainty of the loss tangent in fitting process may yield TB variation less than 4 K [2] and the fluctuation of TSI caused by the distance between the Sun and the Moon can yield TB variation of about ± 2.5 K at the equator region at millimeter-wave channels [25]. Thus, these two uncertainties will not be main reason for the difference of more than 15 K at 157 GHz.

In the simulation of \bar{T}_{BW} , the FWHM of [9] is adopted. It is found that the FWHM has negligible influence on the simulated disk-integrated TB because the FWHM is much larger than the span angle of the Moon. FWHM influences both the numerator and denominator in (20). Fig. 8 shows the simulated \bar{T}_{BW} at 89 GHz with FWHM of 1.2° and 1.162°. The TB difference is about 0.1 K.

In calculation of (11), there are totally 900 subregions on the near-side of Moon surface. But, each subregion is still very huge to contain complicated topography. To take account of the emissivity of each subregion, the digital elevation model (DEM) data with the spatial resolution of 4 pixel/degree is adopted for each subregion. The DEM data were collected by Lunar Orbiter Laser Altimeter onboard the LRO. The mean emissivity from the DEM data of each subregion is used for the \bar{T}_{BW} simulation and compared with the \bar{T}_{BW} of flat facet.

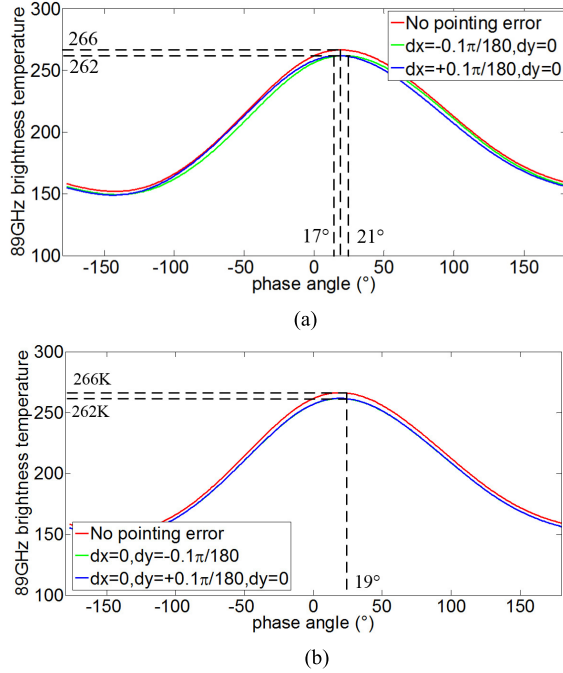


Fig. 9. Influence of pointing error on \bar{T}_{BW} . (a) Horizontal pointing error. (b) Vertical pointing error.

Actually, the final result shows that the TB difference of such DEM modeling of each subregion only causes TB variation of less than 1 K.

More small perturbation in each DEM pixel might present another fine-scale rough surface model. But, due to the lack of measurement, small-scale perturbation cannot be parameterized.

C. Influence of Pointing Error

It has been stated that there is an uncertainty of about 0.3° in the pointing direction in the level 1b data [9]. When there is pointing error, the calculated weighted average TB of the Moon is written as

$$\bar{T}_{BW}^E = \frac{\sum_i (T_{Bi}(\theta_{0i}) - T_{BC}) G_{ip}(dx, dy) \cdot M_i}{\sum_i G_i \cdot M_i} + T_{BC}. \quad (30)$$

To obtain \bar{T}_{BW}^E from (30), it is assumed that the center of the Moon overlaps the center of the DSV. Thus, the G_i on the denominator is given in (21). The $G_{ip}(dx, dy)$ on the numerator is used to present the pointing error

$$G_{ip}(dx, dy) = \frac{1}{2\pi\sigma^2} e^{-\frac{(x_i-dx)^2 + (y_i-dy)^2}{2\sigma^2}} \quad (31)$$

where dx and dy are, respectively, the horizontal and vertical pointing errors, in unit of arc. Fig. 9(a) and (b) gives the influence of $dx = \pm 0.1\pi/180$, $dy = 0$ and $dx = 0$, $dy = \pm 0.1\pi/180$ on disk-average TB at 89 GHz, respectively. The horizontal pointing error of 0.1° may make TB peak decreased by 4–262 K. In addition, the horizontal pointing error may result in a change of $\pm 2^\circ$ in the phase angle of the TB peak. The vertical pointing error of 0.1° may cause TB peak decreased by 4 K and almost have no influence on the phase angle of the TB peak.

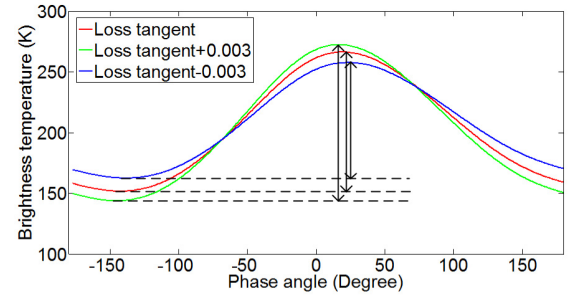


Fig. 10. Influence of loss tangents on \bar{T}_{BW} .

TABLE II
INFLUENCE OF LOSS TANGENTS

Loss tangent	Maximum \bar{T}_{BW}	Minimum \bar{T}_{BW}	$\Delta \bar{T}_{BW}$	Peak \bar{T}_{BW} phase angle
$\tan \delta$	266K	152K	114K	19°
$\tan \delta + 0.003$	273K	144K	129K	17°
$\tan \delta - 0.003$	258K	163K	95K	23°

V. INFLUENCE OF LOSS TANGENTS AND EMISSIVITY

A. Influence of Loss Tangent

The loss tangent described in (16) is validated only at low frequency, that is, 37 GHz. It might need further measurement at higher frequency to modify the loss tangent at the MHS channels.

Fig. 10 shows the simulated \bar{T}_{BW} at 89 GHz for different loss tangent. The red line is calculated with the loss tangent in (16). The loss tangent of the green line is derived by adding 0.003 to (16) while the loss tangent of the blue is derived by subtracting 0.003 from (16). It can be seen that the increased loss tangent may raise \bar{T}_{BW} at daytime and reduce \bar{T}_{BW} at night.

Table II gives the maximum and minimum \bar{T}_{BW} and their difference, and the phase angle of the peak \bar{T}_{BW} is given in Fig. 10. The variation of the loss tangent by 0.006 may cause a variation of 15–19 K in \bar{T}_{BW} .

B. Influence of Emissivity

The emissivity used here is the Fresnel emissivity of flat surface. For example, as the dielectric constant of the regolith surface ranges from 2 to 2.5, the nadir Fresnel emissivity changes from 0.97 to 0.95. Fig. 11 shows the simulated \bar{T}_{BW} with Fresnel emissivity (solid line) and the increased emissivity (imaginary line) by adding 0.02 to the Fresnel emissivity. It can be seen that such a change of the emissivity can make the \bar{T}_{BW} change by 3–6 K.

It is noted that CE-2 37 GHz TB data were observed at nadir observation [2]. As the observation moves to very large angle, the sensitivity of the surface emissivity might need further study.

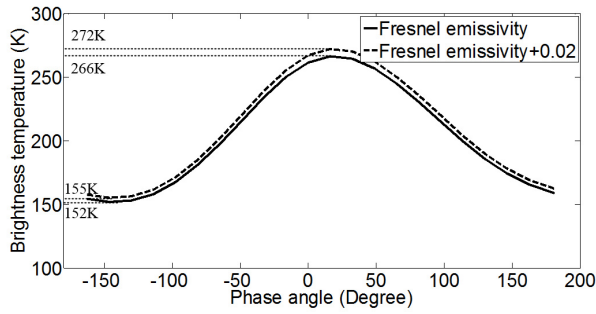


Fig. 11. Influence of emissivity on \bar{T}_{BW} .

VI. CONCLUSION

The Moon maintains good stability in long term and is seen as a potential source for calibration of the satellite-borne radiometers. The advances of the Diviner IR and CE microwave measurements greatly promote quantitative studies of the lunar thermal emission in electromagnetic spectrum. The thermophysical and dielectric properties are applied to modeling, simulation, and data analysis of thermal TB at IR, microwave, and millimeter-wave channels.

As the MHS onboard the NOAA-18 reported the disk-average TB measurements of lunar surface at 89, 157, and 183 GHz [9], this article presents a numerical model and TB simulation in comparison.

Based on the uniformly inhomogeneous half-space model with the thermophysical parameters, for example, bulk density profile, heat capacity profile, and heat conductivity parameters, and the heat conductive equation is solved to obtain the physical temperature profile of regolith media. This approach is validated by the surface temperature from the Diviner data and the temperature at the deep from the Apollo heat experiment measurement. The loss tangents of the regolith media are inversed and validated by CE-2 37 GHz TB. The inversed loss tangent is fit against the TiO_2 abundance.

The whole nearside of the Moon surface is meshed into 900 subregions. Based on integral radiative transfer of the fluctuation dissipation theorem of the half-space model, millimeter-wave TB of regolith media of all subregion and the disk-integrated TB at the MHS three millimeter-wave channels are numerically simulated.

The Moon is taken as an extended target and the antenna temperature of the Moon at the MHS channels is simulated to correct the FWHM and the disk-average TB data. The simulated disk-average TBs are compared with the corrected MHS data [9]. These comparisons and simulation/data analysis reveal feasibility of the Moon as a good and stable calibration source. Future improvements for the Moon thermal calibration, careful design of the observation, and more accurate ground tests are suggested. Summary is listed as follows:

- 1) The phase shifts of the simulated TB peaks at different frequencies are consistent with the MHS TBs observation [9].
- 2) Because of a small penetration depth, high frequency in simulation leads to a small phase delay and a larger \bar{T}_{BW} peak, which is validated by the MHS data at 89 and 183 GHz.

- 3) Although the phase angle of MHS TB peak at 157 GHz lies between that of 89 and 183 GHz, the MHS TB peak of 157 GHz is lower than that of 89 GHz [9]. In addition, more observations at 157 GHz are needed for clarification.
- 4) More observation for the study of the regolith surface parameters, for example, the emissivity at large emission angle and loss tangent at high frequency are needed for further study.
- 5) The integrated MHS TB is sensitive to technical parameters, especially, the FWHM. These parameters also need to be carefully determined.

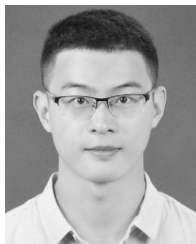
ACKNOWLEDGMENT

The authors would like to thank Dr. M. J. Burgdorf for many useful suggestions. They would also like to thank the anonymous reviewers for their helpful comments.

REFERENCES

- [1] H. Yang *et al.*, "Developing vicarious calibration for microwave sounding instruments using lunar radiation," *IEEE Trans. Geosci. Remote Sens.*, vol. 56, no. 11, pp. 6723–6733, Nov. 2018.
- [2] N. Liu, W. Fa, and Y.-Q. Jin, "Brightness temperature of lunar surface for calibration of multichannel millimeter-wave radiometer of geosynchronous FY-4M," *IEEE Trans. Geosci. Remote Sens.*, vol. 57, no. 5, pp. 3055–3063, May 2019.
- [3] J. H. Piddington and H. C. Minnett, "Microwave thermal radiation from the moon," *Austral. J. Chem.*, vol. 2, no. 1, pp. 63–77, 1949.
- [4] D. A. Paige, "The lunar reconnaissance orbiter diviner lunar radiometer experiment," *Space Sci. Rev.*, vol. 150, pp. 125–160, Oct. 2010.
- [5] A. R. Vasavada, "Lunar equatorial surface temperatures and regolith properties from the diviner lunar radiometer experiment," *J. Geophys. Res.*, vol. 117, no. E12, 2012, doi: [10.1029/2011JE003987](https://doi.org/10.1029/2011JE003987).
- [6] P. O. Hayne, "Global regolith thermophysical properties of the Moon from the Diviner Lunar Radiometer Experiment," *J. Geophys. Res.*, vol. 122, no. 12, pp. 2371–2400, 2017.
- [7] X. Gong, D. A. Paige, M. A. Siegler, and Y.-Q. Jin, "Inversion of dielectric properties of the lunar regolith media with temperature profiles using Chang'e microwave radiometer observations," *IEEE Geosci. Remote Sens. Lett.*, vol. 12, no. 2, pp. 384–388, Feb. 2015.
- [8] T. Fang and W. Fa, "High frequency thermal emission from the lunar surface and near surface temperature of the moon from Chang'E-2 microwave radiometer," *Icarus*, vol. 232, pp. 34–53, Apr. 2014.
- [9] M. J. Burgdorf, S. A. Buehler, I. Hans and M. Prange, "Disk-integrated lunar brightness temperatures between 89 and 190 GHz," *Adv. Astron.*, vol. 2019, Aug. 2019, Art. no. 2350476, doi: [10.1155/2019/2350476](https://doi.org/10.1155/2019/2350476).
- [10] S. Yu and W. Fa, "Thermal conductivity of surficial lunar regolith estimated from lunar reconnaissance orbiter diviner radiometer data," *Planet. Space Sci.*, vol. 124, pp. 48–61, May 2016.
- [11] M. J. Ledlow, "Subsurface emissions from Mercury-VLA radio observations at 2 and 6 centimeters," *Astrophysical J.*, vol. 384, pp. 640–655, Oct. 1992.
- [12] B. S. Hemingway and K. M. R. A. Krupka Robie, "Heat capacities of the alkali feldspars between 350 and 1000 K from differential scanning calorimetry, the thermodynamic functions of the alkali feldspars from 298.15 to 1400 K, and the reaction quartz + jadeite = anabite," *Amer. Mineralogist*, vol. 66, nos. 11–12, pp. 1202–1215, 1981.
- [13] J. A. Fountain and E. A. West, "Thermal conductivity of particulate basalt as a function of density in simulated lunar and martian environments," *J. Geophys. Res.*, vol. 75, no. 20, pp. 4063–4069, Jul. 1970.
- [14] G. D. Racca, "Moon surface thermal characteristics for moon orbiting spacecraft thermal analysis," *Planet. Space Sci.*, vol. 43, no. 6, pp. 835–842, Jun. 1995.
- [15] N. Liu and Y.-Q. Jin, "A real-time model of the seasonal temperature of lunar polar region and data validation," *IEEE Trans. Geosci. Remote Sens.*, vol. 58, no. 3, pp. 1892–1903, Mar. 2020.
- [16] S. J. Keihm, "Interpretation of the lunar microwave brightness temperature spectrum: Feasibility of orbital heat flow mapping," *Icarus*, vol. 60, no. 3, pp. 568–589, Dec. 1984.

- [17] W. Fa and Y.-Q. Jin, "Simulation of brightness temperature from lunar surface and inversion of regolith-layer thickness," *J. Geophys. Res.*, vol. 112, no. E5, May 2007, doi: [10.1029/2006JE002751](https://doi.org/10.1029/2006JE002751).
- [18] W. Fa and M. A. Wiecek, "Regolith thickness over the lunar nearside: Results from Earth-based 70-cm arecibo radar observations," *Icarus*, vol. 218, no. 2, pp. 771–787, Apr. 2012.
- [19] G. Heiken and H. Lunar, *Sourcebook: A User's Guide to the Moon*. New York, NY, USA: Cambridge Univ. Press, 1991, pp. 285–356.
- [20] Y. Q. Jin, *Electromagnetic Scattering Modelling for Quantitative Remote Sensing*. Singapore: World Scientific, 1993, p. 310.
- [21] F. T. Ulaby, R. K. Moore, A. K. Fung, *Microwave Remote Sensing Active & Passive*, vol. 3. Norwood, MA, USA: Artech House, 1986, pp. 1524–1525.
- [22] Q. Huang and M. A. Wiecek, "Density and porosity of the lunar crust from gravity and topography," *J. Geophys. Res.*, vol. 117, no. E5, 2012, doi: [10.1029/2012JE004062](https://doi.org/10.1029/2012JE004062).
- [23] P. G. Lucey, D. T. Blewett, and B. L. Jolliff, "Lunar iron and titanium abundance algorithms based on final processing of clementine ultraviolet-visible images," *J. Geophys. Res.*, vol. 105, no. E8, pp. 20297–20305, Aug. 2000.
- [24] Z. Xu *et al.*, "Two-year cosmology large angular scale surveyor (CLASS) observations: 40 GHz telescope pointing, beam profile, window function, and polarization performance," 2019, *arXiv:1911.04499*. [Online]. Available: <http://arxiv.org/abs/1911.04499>
- [25] N. Liu and Y. Jin, "Calibration of a multichannel millimeter wave radiometer of FY-4M based on the real-time brightness temperature along the lunar equator," *Chin. Sci. Bull.*, vol. 65, nos. 2–3, pp. 185–193, Jan. 2020.



Niutao Liu (Student Member, IEEE) was born in Jiangsu, China, in 1994. He received the B.S. degree from the Department of Telecommunication Engineering, Nanjing University of Posts and Telecommunications, Nanjing, China, in 2016. He is pursuing the Ph.D. degree with the Key Laboratory of Information Science of Electromagnetic Waves, School of Information Science and Engineering, Fudan University, Shanghai, China.

His research interests include planetary remote sensing, computational electromagnetics, and target recognition.



Ya-Qiu Jin (Life Fellow, IEEE) received the B.S. degree in atmospheric physics from Peking University, Beijing, China, in 1970, and the M.S., E.E., and Ph.D. degrees in electrical engineering and computer science from the Massachusetts Institute of Technology, Cambridge, MA, USA, in 1982, 1983, and 1985, respectively.

In 1985, he was a Research Scientist with Atmospheric Environmental Research, Inc., (AER), Cambridge. From 1986 to 1987, he was a Research Associate Fellow with the City University of New York, New York, NY, USA. In 1993, he joined the University of York, York, U.K., as a Visiting Professor, sponsored by the U.K. Royal Society. He is the Te-Pin Professor and the Director of the Key Laboratory for Information Science of Electromagnetic Waves (Ministry of Education), and the Institute of EM Big Data and Intelligence Remote Sensing, Fudan University, Shanghai, China. He has authored more than 800 articles in refereed journals and conference proceedings and 17 books, including *Polarimetric Scattering and SAR Information Retrieval* (Wiley and IEEE, 2013), *Theory and Approach of Information Retrievals from Electromagnetic Scattering and Remote Sensing* (Springer, 2005), and *Electromagnetic Scattering Modelling for Quantitative Remote Sensing* (World Scientific, 1994). His main research interests include electromagnetic scattering and radiative transfer in complex natural media, microwave satellite-borne remote sensing, as well as theoretical modeling, information retrieval and applications in Earth terrain and planetary surfaces, and computational electromagnetics.

Dr. Jin is a fellow of The World Academy of Sciences for Advances of Developing World (TWAS) and International Academy of Astronautics (IAA), and a member of the IEEE GRSS AdCom and the IEEE GRSS Major Awards Committee. He was a recipient of the first-grade MoE Science Prizes in 1992, 1996, and 2009, the China National Science Prize in 1993 and 2011, the IEEE GRSS Education Award in 2010, the IEEE GRSS Distinguished Achievement Award in 2015, the Shanghai Sci/Tech Gong-Cheng Award in 2015, among many other prizes. He was also awarded by the Senior Research Associateship in NOAA/NESDIS by the USA National Research Council in 1996. He is the Academician of the Chinese Academy of Sciences (CAS) and was one of the first groups of the IEEE GRSS Distinguished Speakers. He was the Chair of the IEEE Fellow Evaluation of GRSS from 2009 to 2011, the Co-Chair of TPC for IGARSS 2011 in Vancouver Canada, and the Co-General Chair of IGARSS 2016 in Beijing, China. He was also an Associate Editor of the IEEE TRANSACTIONS ON GEOSCIENCE AND REMOTE SENSING from 2005 to 2012 and IEEE ACCESS from 2016 to 2018.